Comparison of TRMM-Derived Rainfall Products for General and Extreme Rains over the Maritime Continent

ANDUNG BAYU SEKARANOM[a]

Graduate School of Environmental Studies, Nagoya University, Nagoya, Japan

HIROHIKO MASUNAGA

Institute for Space-Earth Environmental Research, Nagoya University, Nagoya, Japan

ABSTRACT

Properties of the rain estimation differences between Tropical Rainfall Measuring Mission (TRMM) Precipitation Radar (PR) 2A25, TRMM Microwave Imager (TMI) 2A12, and TRMM Multisatellite Precipitation Analysis (TMPA) 3B42 are investigated with a focus on distinguishing between nonextreme and extreme rains over the Maritime Continent from 1998 to 2014. Statistical analyses of collocated TMI 1B11 85-GHz polarization-corrected brightness temperatures, PR 2A23 storm-top heights, and PR 2A25 vertical rain profiles are conducted to identify possible sources of the differences. The results indicate that a large estimation difference exists between PR and TMI for the general rain rate (extreme and nonextreme events). The PR–TMI rain-rate differences are larger over land and coast than over ocean. When extreme rain is isolated, a higher frequency of occurrence is identified by PR over ocean, followed by TMI and TMPA. Over land, TMI yields higher rain frequencies than PR with an intermediate range of rain rates (between 15 and 25 mm h^{-1}), but it gives way to PR for the highest extremes. The turnover at the highest rain rates arises because the heaviest rain depicted by PR does not necessarily accompany the strongest ice-scattering signals, which TMI relies on for estimating precipitation over land and coast.

1. Introduction

The Maritime Continent (MC), as introduced by Ramage (1968), defines an archipelagic area over the tropics and is primarily characterized as one of the highest precipitation areas on Earth. The MC covers a wide area that surrounds Southeast Asian countries between the Indian Ocean and the Pacific Ocean, that is, peninsular Malaysia, Singapore, Indonesia, Brunei, Timor, and New Guinea (Qian 2008). Considerable amounts of precipitation occur over the MC because of a combination of complicated environmental factors. One of the most influential components is the existence of warm surface water in the western Pacific Ocean and the eastern Indian Ocean, which are labeled as "warm pools" (Ramage 1968). High evaporation rates over these warm pools provide a large moisture supply around the MC, which subsequently becomes a source of precipitation over the area. However, despite the large moisture supply, precipitation over the MC would be less without an enhancement effect from the Southeast Asian monsoon, which is known as one of the most predominant monsoons in the world (Kripalani and Kulkarni 1997). This monsoon transports moisture from the surrounding ocean directly toward the center of the MC. From December to February, the westerly monsoonal wind dominates and carries abundant moisture from the Indian Ocean, whereas in June through August, the moisture is primarily transported from the Pacific Ocean (Aldrian and Dwi Susanto 2003; Chang et al. 2005). Large amounts of precipitation frequently occur when large volumes of moisture carried by the monsoon reach close to the islands, transported farther to the land particularly during late afternoon and

---

condensed because of a lifting process as a result of the island's mountainous landform (Mori et al. 2004; Ichikawa and Yasunari 2006). Although there are significant variations caused by the local topography, the resulting processes generally yield high precipitation concentrations in the central part of the land (Qian 2008).

The environmental characteristics specific to the MC are responsible not only for the high annual precipitation, which is approximately 1500–3000 mm yr^{-1} over land (As-Syakur et al. 2013), but also for the high frequency of extreme precipitation that can trigger hazards over the MC. An analysis of 11-yr records of global flood frequency in 1998–2008 conducted by Adhikari et al. (2010) shows that Indonesia (which constitutes the largest part of the MC) is listed as one of the top 10 countries for the number of flood events. Several studies have aimed to characterize the environmental factors accompanying the extreme events, and these studies indicated that there are various intraannual and interannual factors involved. For example, an analysis of extreme events over peninsular Malaysia and northern Borneo conducted by Salahuddin and Curtis (2011) from 1998 to 2007 revealed that the combination of the South China Sea circulation and the Madden–Julian oscillation (MJO) is a factor that generates the extreme events. The MJO influence was also identified by Tangang et al. (2008) in peninsular Malaysia during flood events in December 2006 to January 2007, where an active phase of the Indian Ocean dipole was also viewed as another factor responsible for the extremes. However, because of a lack of observations, the general mechanism for the extreme precipitation dynamics over the MC is still not fully understood.

Substantial amounts of precipitation data over the global tropics have been collected through the Tropical Rainfall Measuring Mission (TRMM). The long-term data series (from the end of 1997 to 2014) from the TRMM have enabled the detection of numerous rare events related to precipitation, particularly extreme rainfall. Information regarding various key aspects related to extreme events might be retrieved from rainfall estimates derived from TRMM, particularly from TRMM Precipitation Radar (PR) as an active sensor and TRMM Microwave Imager (TMI) as a passive microwave sensor. PR is the first spaceborne precipitation radar with a 13.8-GHz frequency band with vertical profiling ability in measuring precipitation (Iguchi et al. 2000). Conversely, TMI estimates precipitation based on microwave emissions and ice-scattering signals from precipitating clouds and provides vertical hydrometeor profiles (Kummerow and Giglio 1994; Kummerow et al. 1996).

Because of the different nature of the active and passive sensors in the TRMM, different rain-rate estimations exist among the TRMM-derived rainfall products. Various studies have been conducted to identify the differences in TRMM-derived rainfall products on a global scale by directly comparing the precipitation estimates (Berg et al. 2006; Kumar et al. 2009; Gopalan et al. 2010) or by identifying the factors underlying the differences, for example, based on precipitation water path and precipitation water column (Masunaga et al. 2002). Several studies have highlighted the fundamental causes for the differences. One of the currently known sources of biases comes from the TMI ice-scattering signals. For example, an investigation by Rajendran and Nakazawa (2005) revealed that higher ice-scattering signals are acquired by TMI at mature-to-decaying stages of convection, where the storm-top height is maximum with abundant ice particles. However, these types of events may have low near-surface rain because of a time lag between the processes occurring at the cloud top and the surface (Furuzawa and Nakamura 2005). A comparison study with ground radar data conducted by Zagrodnik and Jiang (2013) showed that TMI has a significant overestimation with respect to ice particles. Very high rain rates are often estimated by TMI at low brightness temperatures, particularly below 220 K, while PR shows a less significant relationship between rain-rate and ice-scattering signals.

In addition to the global comparison, a large number of regional comparison and validation studies have been conducted to analyze the differences, for example, by examining with other satellite products, ground radar, and rain gauge data (Fu and Liu 2003; Prakash et al. 2012). The above studies indicate significant improvements for the most recent TRMM algorithms, and the global rain estimations by PR and TMI show a better agreement, although the regional-scale differences remain large. It has also been suggested that the different estimations emerge because of regional variations of climate characteristics affecting precipitation-related processes (Berg et al. 2006).

The MC's regional characteristics are often described as an area with intense deep convections (Qian 2008). The deep convections are known to have tall cloud structures, with low temperatures at the top and large precipitation amounts at the bottom. Theoretically, the stronger and taller the deep convective structures, the more rain it will produce. However, recently, Hamada et al. (2015) showed that the heaviest rain near the surface is often produced by a system with a relatively low storm height. Using the TRMM PR reflectivity data, they showed that the heaviest rain events occur at a lower PR echo height below the uppermost limit of the
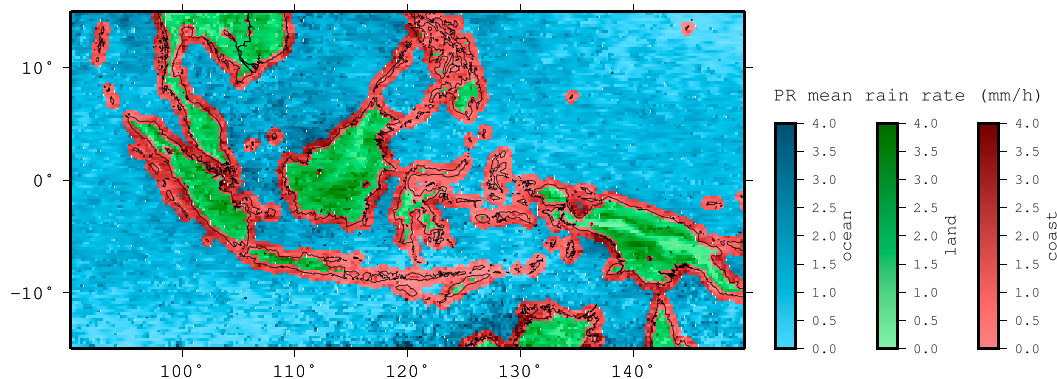
FIG. 1. Map of the study area with classified surface types based on the TMI 2A12 surface flag. Dark shaded colors represent higher mean rain rates from the PR 2A25 near-surface rain averaged from 1998 to 2014.

highest echo height. A more favorable environmental condition at the lower troposphere, where humidity is higher, is suggested as the main reason for the growth of rain drops through collision and coalescence processes. An important implication of their study is that the relation between the cloud microphysics of ice particles aloft and surface rainfall depends systematically on the environmental conditions. This may introduce a potential bias in rainfall estimates between the PR and TMI products, particularly over land.

Although a number of studies have used TRMM data to measure precipitation over the study area, particularly related to the variation of diurnal cycles (Mori et al. 2004; Ichikawa and Yasunari 2006), very few studies have addressed issues related to data comparison and validation with a focus on the MC (As-Syakur et al. 2013), particularly in light of extreme rain events. To this end, this paper presents a comparative analysis of the TRMM-derived precipitation products over the MC, with a focus on extreme rainfall. An outline of the data and methods used in this research are presented in section 2. The statistical comparison results are presented in section 3. These results are discussed further in section 4. A comparison with a focus on the extreme cases is provided in section 5, and the discussion and conclusions related to the main properties of rain-rate estimation differences between each product are presented in section 6.

2. Data and methods

a. Dataset

There are several precipitation estimates from the TRMM, which are primarily derived from PR and TMI. An estimate from combined passive microwave and IR data obtained from the TRMM and other satellites, defined as TRMM Multisatellite Precipitation Analysis (TMPA), is also available (Huffman et al. 2007). This product is based on observations with a finer temporal resolution and global spatial coverage, and thus it enhances the individual measurement capability limited by sporadic overpasses and a finite swath width of hundreds of kilometers. This work focuses on the rain-rate estimation differences among three TRMM-derived precipitation data, namely, PR 2A25 (NASA 2011a), TMI 2A12 (NASA 2011b), and TMPA 3B42 (NASA 2011c). The three precipitation datasets from the TRMM temporal data records of 1998–2014 are examined. Slight changes in the original spatial resolution and swath widths due to an orbit boost in 2001 are considered to be negligible for the present purposes. Only the most recent version of the TRMM products (version 7) is used in this study. The study area is bounded between 15°N and 15°S and between 90° and 150°E, as shown in Fig. 1.

PR 2A25, a TRMM level 2 product, produces instantaneous three-dimensional rainfall structures at 4.3-km (5 km) horizontal resolution and 250-m vertical level within the total swath width of 215 km (247 km) during preboost (postboost) (Iguchi et al. 2000). The vertical profiling ability from PR is augmented with a combination of the Hitschfeld–Bordan method and the surface reference technique (SRT) for estimating the drop size distribution based on radar reflectivity and path-integrated attenuation (PIA) (Iguchi and Meneghini 1994; Seto and Iguchi 2007). The Hitschfeld–Bordan method produces the best estimate at light rain rates, but it fails for high rain rates. Furthermore, this method often generates higher PIA as an effect of the cumulative error from its vertical profiling. In contrast, SRT can produce better results for heavy rain, but it has no vertical information. The combination is achieved by adjusting the PIA from the Hitschfeld–Bordan method with the SRT to obtain optimal estimates.

TMI 2A12, which is also a level 2 product, provides estimations of surface rainfall based on passive

microwave radiometry. The 2A12 product measures instantaneous rain rates based on a given set of brightness temperature inputs from the emission bands (10, 19, 21, and 37 GHz) and 85-GHz ice-scattering bands (Kummerow et al. 1998). The TMI finest horizontal resolution is approximately 5 km × 12 km, which is larger than PR. The TMI swath is nearly 3 times as wide as the PR swath (approximately 878 km after orbit boost in August 2001). There are different streams in the TMI algorithm for estimating surface rainfall depending on the surface types of ocean, land, and coast. Over ocean, the algorithm utilizes all the nine channels, including the emission and ice-scattering channels to retrieve rain rates. In contrast to the ocean algorithm, the land and coast algorithms are only able to estimate rain rates based on the 85-GHz ice-scattering channel to avoid the large uncertainty in the microwave surface emissivity (Kummerow et al. 2001). Therefore, it is challenging to accurately estimate rain rates over land and coast, which is a major weakness of TMI.

TMPA 3B42 is one of the level 3 TRMM products, which produces adjusted merged passive microwave–infrared (IR) precipitation at the global scale with 0.25° × 0.25° spatial resolution and 3-hourly temporal resolution (Huffman et al. 2007). The global coverage (up to 50°S–50°N) and a fine temporal resolution are achieved by combining input from several data providers, namely, 1) level 1 TRMM TMI brightness temperature (2A12), 2) level 2 PR–TMI combined rainfall profile (2B31), 3) NSIDC level 2 AMSR-E precipitation estimate, 4) NOAA/NCDC M-CLASS SSMIS brightness temperature, 5) NOAA/NCDC CLASS SSMIS antenna temperature, 6) NESDIS Microwave Surface and Precipitation Products System (MSPPS) level 2 AMSU-B precipitation estimate, 7) NESDIS MSPPS operational level 2 Microwave Humidity Sounder (MHS) precipitation estimate, 8) NOAA/NCDC level 3 Gridded Satellite (GridSat-B1) IR brightness temperature, and 9) NOAA/NWS/CPC merged 4-km geostationary satellite IR brightness temperature (Huffman and Bolvin 2013). The 3B42 final product is later obtained by further calibrating the data with GPCC level 3 precipitation gauge analysis on a monthly basis to generate more accurate estimates than the near-real-time product, and it is released approximately two months later.

The minimum rain rate differs among the products. The minimum PR echo detectability is approximately 17 dBZ (Iguchi et al. 2000), close to 0.5 mm h^{-1}. The latest version of the TMI algorithm (version 7) removes the screening process over ocean and provides rain probability parameters, with a minimum detectability of 0.4 mm h^{-1} (Zagrodnik and Jiang 2013). Although no specific detectability threshold is given for TMPA, it is considered to be a less reliable method for determining light rain fields. Low IR cloud temperatures, but no surface rain, can be mistaken as rain fields by TMPA, particularly because of the existence of ice particles from cirrus clouds or decaying precipitation systems (Rosenfeld 2007).

b. Data preprocessing

Because of differences in area coverage and spatial and temporal resolutions among the three products, a direct comparison among these data is impossible in the original format of each dataset; therefore, a data preprocessing routine is required. In this research, we consider the data only in which a PR swath exists, neglecting the TMI and TMPA data falling outside the PR field of view because the PR swath is narrowest. The omission of any measurements outside the PR swath leads to a bias in evaluating the range of sensors contributing to the TMPA because its design does not usually allow non-TRMM satellites in the zone that the PR covers. As such, the present strategy is somewhat of limited utility for evaluating the TMPA rainfall. A more thorough assessment of TMPA would require the whole TMPA fields to be analyzed at the expense of the loss of sampling consistency with PR and TMI overpasses. Such an extensive analysis is outside the scope of the present study.

Since the spatial resolution is approximately 5 km × 5 km for PR, 5 km × 12 km for TMI, and 0.25° × 0.25° for TMPA (approximately 28 km × 28 km in the study area), a spatial averaging technique is implemented. We average a set of pixels from PR and TMI data located within each TMPA grid to match the TMPA since it has the coarsest resolution. The different temporal resolutions between instantaneous rain rates from PR and TMI and 3-h rain rates from TMPA could also produce a temporal mismatch in the analysis. To mitigate the mismatch, the time records of PR and TMI overpasses closest to the 3-hourly time stamp of TMPA are selected and stacked together into a single time bin. Thus, the comparison between the three data is calculated for each 3-h time bin, which contains a single overpass for each of the three products. The maximum temporal difference allowed between TMPA and the two products in each calculated bin falls within a range from −1.5 to 1.5 h. This time range is considered to reasonably capture extreme rain events in the study area where extreme events often occur in a duration of approximately about 5 h for rain rates higher than 15 mm h^{-1} (approximately equal to the uppermost 1% PR threshold) (Liu et al. 2015).

In addition to the spatial and temporal differences, there is also a difference in how each pixel is categorized as rain or nonrain from PR and TMI. In general, there

are three main groups of nonrain/rain flag classifications from PR, consisting of no-rain, rain-possible, and rain-certain fields (TRMM PR Team 2011). A pixel is classified as rain in PR when its echo exceeds a certain threshold. Furthermore, when the echo is weak but higher than the threshold or when it is possibly influenced by clutter contamination, it is labeled as a rain-possible field. Since the minimum rain-rate detectability is approximately $0.5 \, \mathrm{mm \, h^{-1}}$ ($\sim 17 \, \mathrm{dB}Z$) from PR and considerably less for TMI, we set this value as the threshold for determining no-rain/rain fields. Thus, only grids with a rain rate higher than $0.5 \, \mathrm{mm \, h^{-1}}$ are considered as raining.

This study treats ocean, land, and coast separately since different surface types potentially becomes a source of error in the estimation. This separation is intended to address the different modes of the TMI algorithm depending on the surface types, especially because of the limitation of the land algorithm in using emission channels. The surface type classification is assigned for each grid from the matched-up dataset based on the TMI 2A12 surface flag. However, since the spatial resolution of the matched-up dataset is different from the original TMI spatial resolution, the grid surface types are determined based on the dominant TMI surface type with each grid box. If more than two-thirds of a grid box is filled with TMI land pixels, then that grid box is classified as land surface and vice versa for ocean. A grid box that is identified as neither land or ocean is defined as coast.

c. Statistical intercomparison

The preprocessing routine described in the previous section generates a combined dataset that consists of PR, TMI, and TMPA rain estimates with a $0.25° \times 0.25°$ spatial resolution and 3-hourly temporal resolution. First, the three datasets are compared in terms of the domain-mean climatology over a range from very light rain to the heaviest rain. We focus on the relative differences among the products, and no ground-based observation data are utilized for the validation.

The mean rain rate is computed in two different manners: conditional and unconditional rain rates. The conditional means are calculated with raining grid boxes only (grid with rain rate $> 0.5 \, \mathrm{mm \, h^{-1}}$), while the unconditional means represent the average of all grid boxes irrespective of raining or nonraining. The mean values are obtained separately for different surface types of ocean, land, and coast–mixed surfaces. We also study the potential difference in moderately or extremely heavy rainfall using several rain-rate thresholds. Eight thresholds of $0.5, 1, 5, 10, 15, 20, 30,$ and $40 \, \mathrm{mm \, h^{-1}}$ are examined, below which all rain rates are excluded.

Second, differences in the rain-rate estimation is assessed in further detail between each pair among the three products, that is, PR–TMI, PR–TMPA, and TMI–TMPA. Absolute nonrain events, in which both of the values are equal to $\leq 0.5 \, \mathrm{mm \, h^{-1}}$, are excluded from the analysis. The dissimilarities between the first and second data from each pair are computed to identify a positive or negative difference value. This positive (negative) difference value implies that a higher (lower) rain-rate estimation exists from the first data to the second data in a pair based on the following function:

$$D = \frac{1}{n} \sum_i (R_{x,i} - R_{y,i}), \tag{1}$$

where D is the difference values, n is the total number of data, $R_{x,i}$ and $R_{y,i}$ are the first and second data in each pair, and i denotes the individual data samples.

A few additional analyses of the difference values are conducted to account for the fact that rain screening is not homogeneous across the three products. Following Habib et al. (2009) and Zagrodnik and Jiang (2013), we calculate the hit signal difference (HD), miss signal difference (MD), and false signal difference (FD). The HD is calculated when both the first and the second data in a pair contain a finite rain rate within the same grid box:

$$HD = \frac{1}{n} \sum_i (R_{x,i,H} - R_{y,i,H}), \tag{2}$$

where HD is the hit signal difference, and $R_{x,i,H}$ and $R_{y,i,H}$ are the first and second rain data samples for $R_{x,i} > 0$ and $R_{y,i} > 0$. The MD is calculated with the samples where the first data misses the rain events detected by the second data in a pair:

$$MD = \frac{1}{n} \sum_i R_{y,i,T}, \tag{3}$$

where MD is the miss signal difference, and $R_{y,i,T}$ is the second data samples for $R_{x,i} > 0$ and $R_{y,i} > 0$. The FD is defined as the inverse to the MD:

$$FD = \frac{1}{n} \sum_i R_{x,i,T}, \tag{4}$$

where FD is the false signal difference, and $R_{x,i,T}$ is the first data samples for $R_{x,i} > 0$ and $R_{y,i} > 0$.

Subsetting each data pair only for the HD component, the conditional root-mean-square difference (RMSD) is calculated and decomposed into its systematic and random differences (Habib et al. 2009; Zagrodnik and Jiang 2013):

$$\text{RMSD} = \text{RMS}D_s + \text{RMSD}_r = \sqrt{\frac{1}{n}\sum_i (R_{x,i} - R_{y,i})^2},$$

$$(5)$$

where RSMD_s is systematic difference, RSMD_r is random difference, and n is total number of the data in a pair with rain rate $> 0.5\,\text{mm h}^{-1}$. The systematic error is extracted by linear regression as

$$\text{RMSD}_s = \sqrt{\frac{1}{n}\sum_i (R'_{x,i} - R_{y,i})^2},$$

$$(6)$$

where $R'_{x,i} = a + b \times R_{y,i}$ and a and b are the regression constants.

Finally, the exceedance probability distribution is utilized to assess the interproduct differences in extreme rainfall. The exceedance values represent the occurrence probability at or above a certain rain rate, following the formula

$$P = m/(n + 1),$$

$$(7)$$

where P is the exceedance probability, m is the data rank ordered from the highest rain rate to the prescribed threshold of rain rate, and n is the total number of each data.

d. Extreme rainfall analysis

In this study, extreme rainfall is examined in terms of passive microwave ice-scattering signals, radar storm-top heights, and vertical rain profiles. Those parameters are useful to characterize clouds with extreme precipitation, particularly for the case of deep convections. A strong deep convective cloud, expected to be heavily precipitating, generally contains a large amount of ice particles. The microwave scattering due to such ice particles would not only produce a striking decrease in the measured TMI 85-GHz brightness temperature but result in a notable PR echo-top height. In this study, the 85-GHz brightness temperature data from TMI 1B11 (NASA 2011d), storm-top height data from PR 2A23 (NASA 2011e), and vertical rain profile data from PR 2A25 are utilized. All of the data are gridded as previously described.

There are various methods for categorizing nonextreme and extreme rain events. For example, Salahuddin and Curtis (2011) categorized extreme events based on fixed thresholds of 10, 20, and 40 mm for the entire study area. Hamada et al. (2015) defined the uppermost 0.1% data distribution at each $2.5° \times 2.5°$ as extreme events. Furthermore, because of large variations accompanying different classification methods, Kiktev et al. (2003) used multiple classification methods to define the extremes,

such as fixed thresholds, regional uppermost values, and annual maximum values. In this work, extreme rain events are defined as the uppermost 1% from the data over the entire region. It is assumed that regional variations of extreme rainfall are relatively small because of the uniform climate characteristics of the study area.

Ice-scattering signals in the TMI 85-GHz brightness temperature are a proxy of heavy convective rainfall over all three surfaces, although such signals are more heavily relied upon over land than over ocean. Differences between PR and TMI estimation that arise from the ice-scattering signal have also been reported, particularly between deep convection and warm rain events (Nesbitt et al. 2000; Zagrodnik and Jiang 2013). Regarding this issue, we identify the extremes as a function of polarization-corrected brightness temperature (PCT), which is calculated based on the vertical and horizontal 85-GHz brightness temperatures received by TMI (Spencer et al. 1989):

$$\text{PCT} = 1.818 T_{\text{BV}} - 0.818 T_{\text{BH}},$$

$$(8)$$

where PCT is the polarization-corrected brightness temperature, T_{BV} is the vertically polarized brightness temperature, and T_{BH} is the horizontally polarized brightness temperature at TMI 85 GHz. For identifying the extremes as a function of PCT, the definition of extreme in this research is slightly different than the general definition. In this research, an extreme is derived from the uppermost 1% of rain events at each 5-K PCT bin.

3. Intercomparison of mean, difference value, and RMSD

The results of mean, difference value, and RMSD analyses are presented in this section. Approximately two-thirds of the study domain is ocean (66.14%), while the remainder is coast (22.77%) and land (11.09%) (Table 1). A comparison of the unconditional and conditional means for each surface type is presented in Table 1. This table shows that TMPA has the highest unconditional mean when compared with PR and TMI for all surface types, that is, 0.21, 0.32, and 0.23 mm h^{-1} for ocean, land, and coast, respectively. In contrast to the unconditional mean, TMPA has the lowest value for any surface type as observed from the conditional mean. TMI tends to produce the highest conditional means when compared with PR and TMPA. The TMI conditional mean for land is 2.74 mm h^{-1} and for coast is 2.55 mm h^{-1}, while PR produces the highest conditional mean over ocean (2.41 mm h^{-1}). The differences between PR–TMI conditional means are further

TABLE 1. Total number of grid boxes (including nonraining grids), unconditional mean (average of all grid boxes $\geq 0\,mm\,h^{-1}$), and conditional mean (average of all grid boxes for $>0.5\,mm\,h^{-1}$) based on each surface type.

	Total number of grid boxes			Unconditional mean			Conditional mean		
	Ocean	Land	Coast	Ocean	Land	Coast	Ocean	Land	Coast
PR				0.19	0.28	0.20	2.41	2.55	2.48
TMI	14 578 000 (66.14%)	2 444 200 (11.09%)	5 019 500 (22.77%)	0.17	0.26	0.14	2.04	2.74	2.55
TMPA				0.21	0.32	0.23	1.97	2.40	2.41

investigated based on its original pixel-by-pixel standard deviations within each TMPA grid resolution. The PR standard deviations for ocean, land, and coast are 3.60, 3.87, and 3.82, while TMI standard deviations are 1.67, 2.59, and 2.55. In general, PR yields higher rain-rate variations than TMI within the $0.25° \times 0.25°$ grid resolution. It is possible that rain events detected by PR contain smaller precipitating areas than TMI because the PR swath is narrower than the TMI swath.

To obtain more detailed information than the mean values from all rain rates, it is useful to identify the rain occurrence above specific rain-rate thresholds as a fraction of the total number of observations, as shown in Table 2. A comparison of rain frequencies over ocean, land, and coast shows that generally, the land surface often has the highest rain frequency. As identified by

Qian (2008), this contrast likely results from the strong afternoon heating over land that draws large moisture flux from the ocean, which then condenses into rain in the central part of the islands. The rain rate remaining the highest over land holds for light rain to heavy rain from >0.5 to $>20\,mm\,h^{-1}$. Furthermore, this table also provides support for the previous result related to the large number of very light rain rates identified by TMPA. In this case, TMPA has a higher frequency for very light rain rates (>0.5 and $>1\,mm\,h^{-1}$) but decreases to less than PR and TMI for the higher thresholds ($>5\,mm\,h^{-1}$ and above). At the middle-to-upper range, PR tends to identify a higher number of rain events relative to the other two estimates. The higher PR frequency is particularly found over ocean and coast from rain rates > 5 to $> 40\,mm\,h^{-1}$ thresholds. In contrast to PR, TMI tends to identify higher rain frequencies for medium to heavy rain over land, from >10 to $>30\,mm\,h^{-1}$. Although this table can define the general characteristics of rain frequencies, a closer look at each specific rain rate is required. A detailed analysis was obtained by further elaboration with a more comprehensive statistical analysis based on cumulative contribution, as presented in the next section.

The result of difference value analysis (HD, MD, and FD) is presented in Table 3, and the RMSD between each pair of products is shown in Table 4. Both of the analyses show that PR–TMI often produces the largest difference when compared with the other data pairs,

TABLE 2. Percentage of grid boxes for rain rate > 0.5 to $> 40\,mm\,h^{-1}$ based on each algorithm and surface type. Surface maximums are displayed in bold font.

Number of grid boxes	Surface	Percent of total data		
		PR	TMI	TMPA
$>0.5\,mm\,h^{-1}$	Ocean	8.0149	8.2439	**10.8422**
	Land	10.9565	9.3488	**13.1510**
	Coast	8.1611	5.4697	**9.3435**
$>1\,mm\,h^{-1}$	Ocean	5.0773	4.81	**6.7406**
	Land	7.5153	6.8109	**9.0515**
	Coast	5.4264	3.8474	**6.2759**
$>5\,mm\,h^{-1}$	Ocean	**0.9077**	0.6744	0.7026
	Land	1.3362	1.2065	**1.3944**
	Coast	0.9631	0.6585	**1.0307**
$>10\,mm\,h^{-1}$	Ocean	**0.2329**	0.1208	0.1173
	Land	0.3019	**0.3731**	0.2833
	Coast	**0.2380**	0.1393	0.2133
$>15\,mm\,h^{-1}$	Ocean	**0.0901**	0.0394	0.0267
	Land	0.0869	**0.1330**	0.0734
	Coast	**0.0871**	0.0452	0.0684
$>20\,mm\,h^{-1}$	Ocean	**0.0335**	0.0167	0.0089
	Land	0.0392	**0.0468**	0.0217
	Coast	**0.0272**	0.0152	0.0226
$>30\,mm\,h^{-1}$	Ocean	**0.0060**	0.0048	0.0019
	Land	0.0041	**0.0055**	0.0026
	Coast	**0.0051**	0.0020	0.0035
$>40\,mm\,h^{-1}$	Ocean	**0.0013**	0.0011	0.0005
	Land	**0.0007**	0.0004	0.0006
	Coast	**0.0012**	0.0002	0.0007

TABLE 3. Cross matrix of HD, MD, and FD of rain rate between each pair out of the three algorithms ($mm\,h^{-1}$). The results are classified based on each surface type from left to right. The HD, MD, and FD are shown from top to bottom. The highest difference for each surface is displayed in bold font.

		Ocean		Land		Coast	
		TMI	TMPA	TMI	TMPA	TMI	TMPA
HD	PR	**0.43**	0.09	0.09	−0.05	0.63	−0.05
	TMI	—	−0.30	—	**−0.20**	—	**−0.77**
MD	PR	−0.88	**−0.92**	**−1.37**	−1.22	−1.27	−1.21
	TMI	—	−0.82	—	−1.06	—	**−1.44**
FD	PR	**0.90**	0.79	**1.22**	0.86	**1.33**	0.87
	TMI	—	0.61	—	0.74	—	0.73

TABLE 4. Cross matrix of conditional RMSDs and the contribution of systematic RMSD$_s$s (mm h^{-1}) between each algorithm (for rain rate > 0.5 mm h^{-1}). The highest RMSD at each surface is displayed in bold font.

		Ocean		Land		Coast	
		TMI	TMPA	TMI	TMPA	TMI	TMPA
RMSD	PR	**2.01**	1.62	**2.67**	1.98	**2.57**	2.00
	TMI	—	1.36	—	1.92	—	1.95
RMSD$_s$	PR	0.35	0.29	**1.35**	0.57	1.04	0.61
	TMI	—	**0.44**	—	0.49	—	**1.19**

regardless of surface types. The PR–TMI high MD and FD imply that the majority of the differences are closely related to the nonrain and rain classifications by each product. Based on the conditional RMSD, TMI–TMPA is the smallest in the total RMSD for all three surfaces (1.36, 1.92, and 1.95 mm h^{-1} for ocean, land, and coast, respectively). However, the systematic component of the RMSD shows that the difference between PR and TMPA is smaller over ocean and coast.

4. Rain-rate contribution

This section presents an analysis of the probability distribution of rainfall in terms of cumulative probability, exceedance probability, and mean rain rate as a function of the TMI 85-GHz PCT.

The first result, shown in Fig. 2, provides the cumulative probability contribution among the three datasets. The main feature is that PR provides the smallest contribution to low and medium rain rates when compared with TMI and TMPA. The contribution of rain rate from the minimum up to 10 mm h^{-1} is approximately 70%–80% for PR, while higher contributions are achieved by TMI and TMPA in the same range. The TMPAfs cumulative contribution is higher than PR and TMI for any

given rain-rate value, particularly over ocean and land. The higher cumulative contribution is possibly generated by a large number of light rain events, which are responsible to the TMPAfs low conditional means shown in Table 1. The TMI contribution, when compared with TMPA, shows a similar pattern. However, TMI has a smaller contribution than TMPA for low-to-medium rain rates, particularly over land. The TMI contribution is approximately 80% at 10 mm h^{-1} over land, which is close to PR. Over coast, the TMI contribution is consistent with TMPA.

The exceedance probability is presented in Fig. 3. The result indicates that PR generally produces a higher exceedance probability than TMI and TMPA over ocean and coast. This result provides an explanation for Table 2, where PR identifies a higher number of rain events >10 and >20 mm h^{-1} over ocean and coast than the other two datasets, while TMI is higher over land. It appears that the TMI land algorithm produces a higher exceedance probability than PR between 10 and 25 mm h^{-1}. However, the TMI exceedance probability rapidly decreases after >25 mm h^{-1}. This result is further examined in section 5.

Figure 4 shows a comparison of the mean rain rate as a function of TMI 85-GHz PCT. Over land, all the algorithms produced similar results when TMI 85-GHz PCT > 200 K, while for lower PCTs, TMI tends to show higher rain rates than the other two datasets. The higher TMI rain rate below 200-K PCT is also observed over coast, but the spread occurs at lower PCT (at approximately 160 K). This spread presumably explains why TMI exhibits a higher frequency of rain events for a rain rate of >10 mm h^{-1}. It could be implied that the higher exceedance probability of TMI over land shown in Fig. 3 is due to the frequent rain events with PCTs below 240 K. The excess of TMI rain for low PCTs is not observed over ocean, which may be expected because
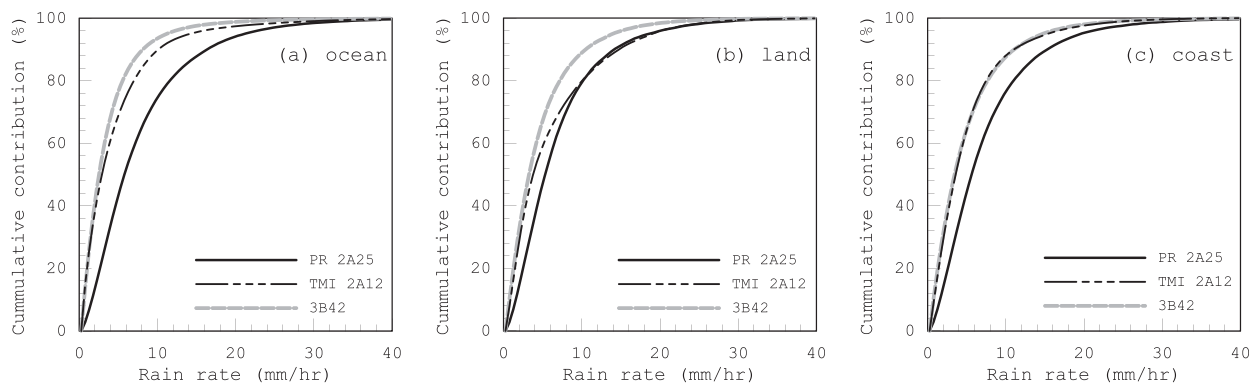

FIG. 2. Cumulative contribution to mean rain rate (%) from PR (solid black line), TMI (dashed black line), and TMPA (dashed gray line) for (a) ocean, (b) land, and (c) coast, calculated from each 0.25° square grid from 1998 to 2014.
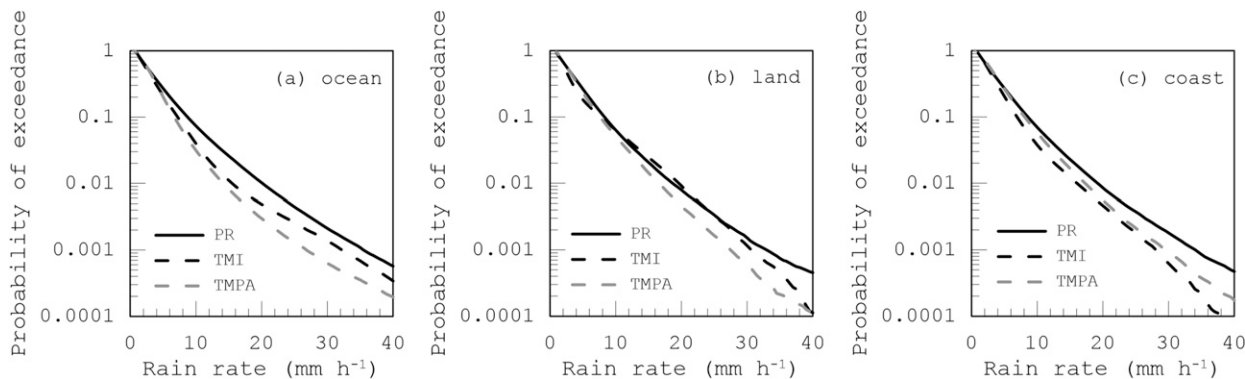
FIG. 3. Probability of exceedance for PR (solid black line), TMI (dashed black line), and TMPA (dashed gray line) based on each 0.25° square grid from 1998 to 2014. A rain rate with corresponding exceedance value close to 1 indicates a higher probability to occur. The plots represent each surface: (a) ocean, (b) land, and (c) coast.

the TMI land algorithm relies entirely on the ice-scattering channels.

5. Comparison of extreme rainfall

The previous result in Fig. 4 shows that the ice scattering may not be tightly linked to the surface rainfall. In particular, the TMI land algorithm is known for being insensitive to light rain without ice particles (Furuzawa and Nakamura 2005; Rajendran and Nakazawa 2005; Zagrodnik and Jiang 2013). The apparent inconsistency between the exceedance probability plot (Fig. 3b) and rain-rate–PCT plot (Fig. 4b) over land is further investigated in this section. Figure 5 presents a two-dimensional histogram of rain rate and TMI PCT. The relationship between rain rate and PCT is broadly spread except for the TMI land and coast, in which the rain rate is tightly correlated with PCT. This result is likely because the TMI land and coast algorithms do not rely on the emission channels. Although the mean rain

rate as a function of PCT (shown as black plus signs in Fig. 5) indicates that the TMI land and coast algorithms are higher than PR and TMPA at an intermediate rain range, the histogram shows that the TMI rain–PCT curve over land and coast rarely contains rain rates higher than $20 \, \text{mm h}^{-1}$ except at the lowest PCTs. However, PR rain can exceed $20 \, \text{mm h}^{-1}$ over a wide range of PCTs over the three surfaces.

Figure 6 shows the PCT–rain relation as plotted in Fig. 4 but calculated from the samples limited to the uppermost 1% rain rate. PR consistently has the highest rain rate for all PCTs over land and coast when compared with TMI and TMPA. This result is in contrast with the mean rain-rate–PCT plot presented in Fig. 4, where TMI is the highest over land for an intermediate range of rain rates when compared with the two other datasets. Comparison of the two figures shows that there are differences related to the range of the data distribution inside the TMI land algorithm, especially between the mean and the uppermost values as a function of PCTs.
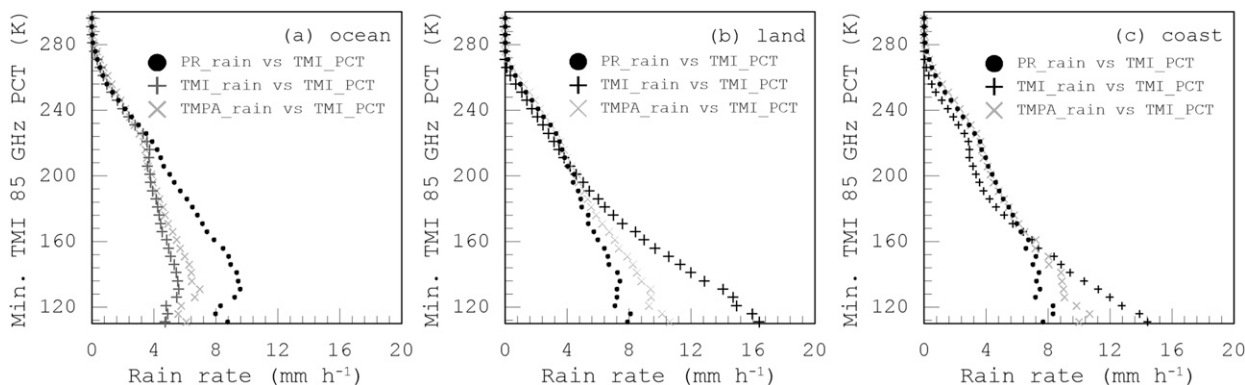

FIG. 4. Plots of TMI minimum 85-GHz PCT vs averaged rain rate from PR (filled circles), TMI (plus signs), and TMPA (times signs). The PCT values are obtained from the minimum value inside collocated 1/4° square grid boxes from 1998 to 2014. Each point represents the mean value for a 5-K PCT bin. The result is classified into three surface types: (a) ocean, (b) land, and (c) coast.
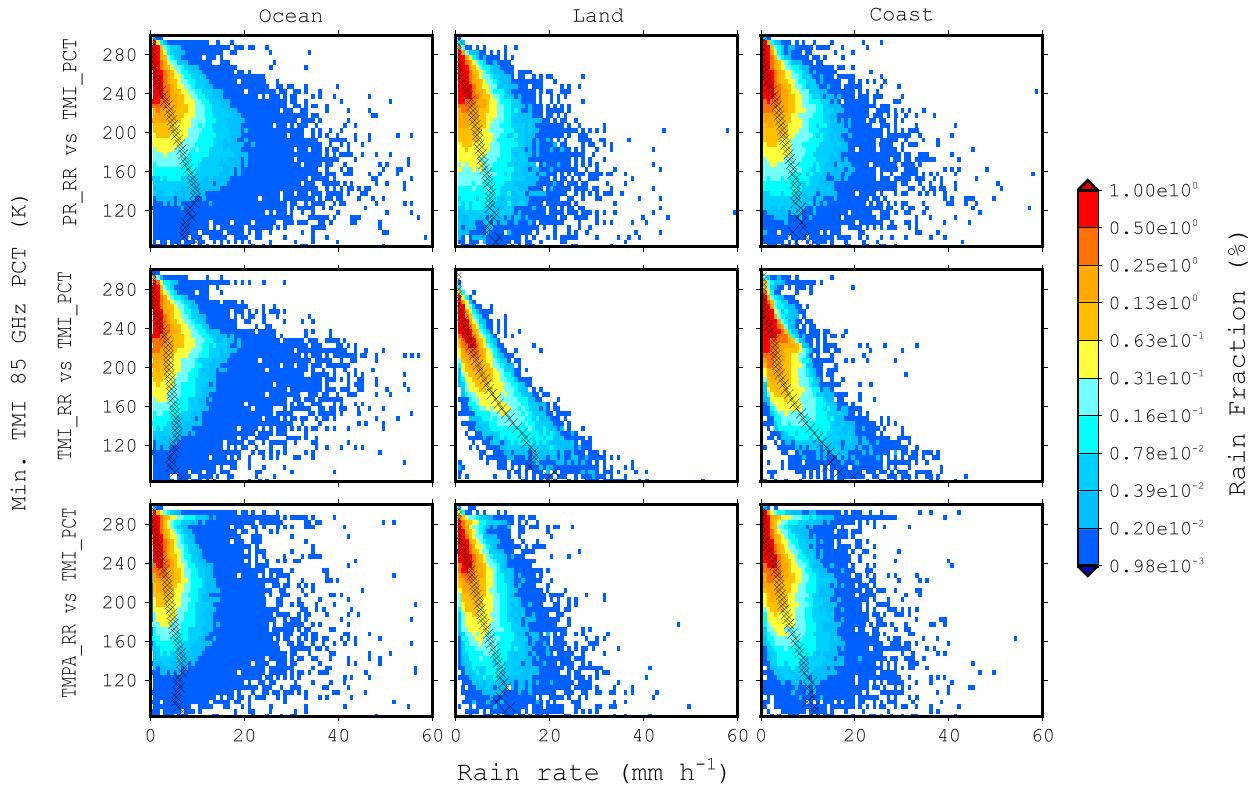
FIG. 5. Fraction of the total number of rain events as a function of rain rates and TMI minimum 85-GHz PCTs, obtained from collocated ¼° square grid boxes from 1998 to 2014. The data are classified by the (top) PR, (middle) TMI, and (bottom) TMPA algorithms and the (left) ocean, (center) land, and (right) coast surface types. The scale represents fractions of the total data for each plot.

A remaining question is, as shown in Fig. 5, why are the heaviest rains detected by PR not necessarily associated with the lowest TMI PCTs? To address this question, we examine the storm-top heights from collocated PR 2A23 associated with extreme rain rates of the uppermost 1% for each PCT bin in Fig. 7. The result indicates that PR, TMI, and TMPA could produce comparable results over ocean. As identified by the three estimates, the storm-top height is from approximately 6 km at $10\,\mathrm{mm\,h^{-1}}$ to

approximately 8–10 km at $30\,\mathrm{mm\,h^{-1}}$ over ocean. However, it appears that TMI yields a higher storm-top height for any given rain rate over land and coast relative to PR and TMPA. Over land, TMI indicates storm-top heights from approximately 8 km at $10\,\mathrm{mm\,h^{-1}}$ to 12 km at $30\,\mathrm{mm\,h^{-1}}$. The extreme events derived from PR and TMPA, in contrast, exhibit lower storm-top heights over land: from approximately 5 km at $10\,\mathrm{mm\,h^{-1}}$ to 10 km at $30\,\mathrm{mm\,h^{-1}}$. Because TMI does not directly observe
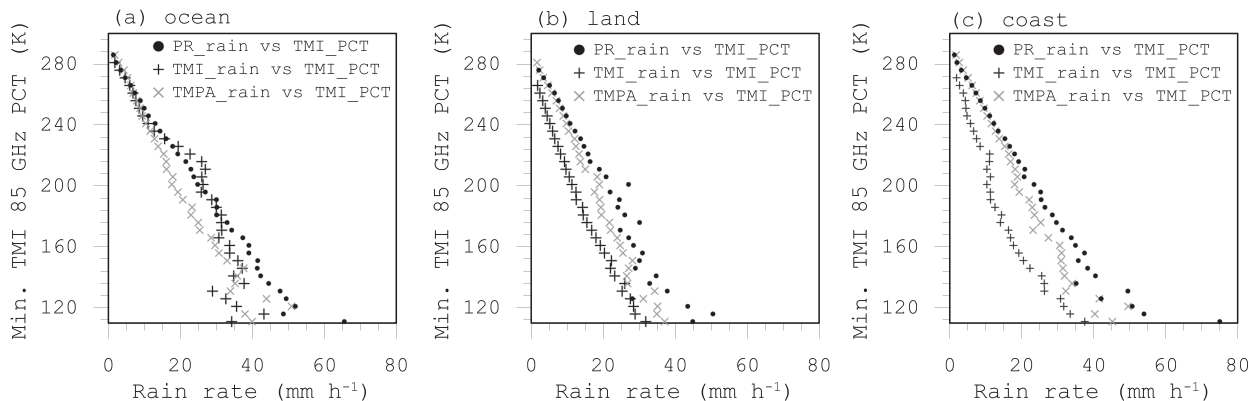

FIG. 6. As in Fig. 4, but for the average of the uppermost 1% rain rate at each 5-K 85-GHz TMI minimum PCT bin.
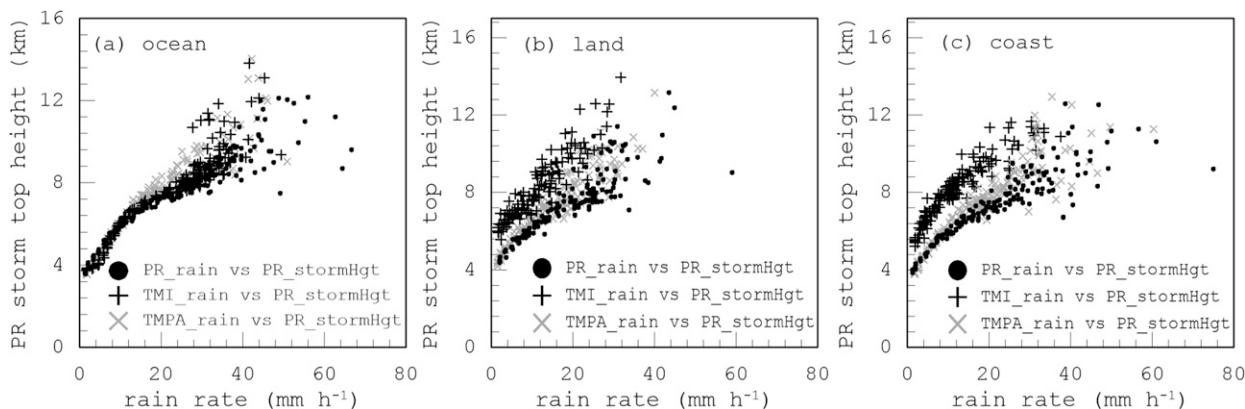
FIG. 7. Plots of collocated PR storm-top height as a function of the uppermost 1% rain rates from PR (filled circles), TMI (plus signs), and TMPA (times signs). The uppermost 1% are obtained using TRMM observations from 1998 to 2014. The storm-top height data are obtained from the average value of collocated PR2A23 at $1/4°$ square grid boxes and classified into (a) ocean, (b) land, and (c) coast.

surface rain rates but rather relies on the empirical relationship with ice-scattering signals, this relationship may be somewhat too exaggerated (i.e., excessive ice scattering for a given surface rain rate) for extreme rainfall.

The relation of surface rain with PCT is further examined in terms of vertical rain profiles for 1% extreme rainfall. Figure 8 shows the PR vertical rain profiles averaged within the extreme subset identified by PR (red), TMI (green), and TMPA (blue) while considering the PCT values. The plots are categorized into four PCT ranges: <160, 160–200, 200–240, and >240 K. Over ocean, the vertical profiles agree well among the three products for all PCT ranges. At the lowest 85-GHz PCTs (<160 K), the near-surface rain reaches approximately 22–23 mm h^{-1}. The near-surface rain rates are decreasing at higher PCTs: approximately 15, 10, and 3 mm h^{-1} for 160–200-, 200–240-, and >240-K PCTs, respectively. Over land, the vertical rain profiles disagree among the products as compared with over the ocean. The PR-identified extreme rain profiles exhibit a significant increase in rain rate from 5 km to near the surface. In contrast, such a downward increase is more modest for the TMI-identified extremes. This PR–TMI difference resulted in the TMI's lower near-surface rain. For PCTs <160 K, the near-surface rain rate is approximately 12–13 mm h^{-1} when extremes are defined by PR, while the surface rain rate reaches only approximately 10 mm h^{-1} for the TMI-sorted subset. This kind of difference is also found for PCTs of 160–200 and 200–240 K. Comparison of the vertical rain profiles over the coast also indicates differences that are similar to those over land.

One might wonder whether the present statistics from MC precipitation are also representative of global rainfall characteristics. To address this question, we present the results of exceedance probabilities obtained from the global tropics and a few representative regions across the tropics (Fig. 9). The global exceedance probabilities (with MC excluded), as shown in Figs. 9a and 9b, imply that a similar condition also exists on a global scale. Over global land, the TMI probability is slightly higher than the PR probability at midrange extremes (approximately 15–30 mm h^{-1}). Although the pattern is similar, MC has a higher PR probability above 30 mm h^{-1}, while the TMI probability rapidly decreases at lower rain rates than the global average. Nevertheless, the overall characteristics found previously for MC also apply to the global tropics.

The exceedance probability with four other regions is also shown in Fig. 9. Plots of ocean probabilities are represented by east Pacific (Fig. 9c) and west Pacific (Fig. 9d), while land is represented by South America (Fig. 9d) and central Africa (Fig. 9f). The probabilities are homogeneous over ocean but have large variations over land. The plot over South America produces a higher PR probability at all ranges when compared with the TMI, and it yields a different pattern than that observed for MC over global land. Central Africa shows a contrasting result, in which the TMI probability is higher than PR for rain rates higher than 10 mm h^{-1}. The PR exceedance probability over central Africa in this case is lower than the PR exceedance probability at the global scale. The regional contrast suggests that South America provides a relatively oceanic environment for precipitation to develop, while Africa is under a highly continental condition (Masunaga et al. 2005).

6. Conclusions and discussion

The results of this study highlight the properties of different rain-rate estimation among PR, TMI, and TMPA over MC for both nonextreme and extreme cases
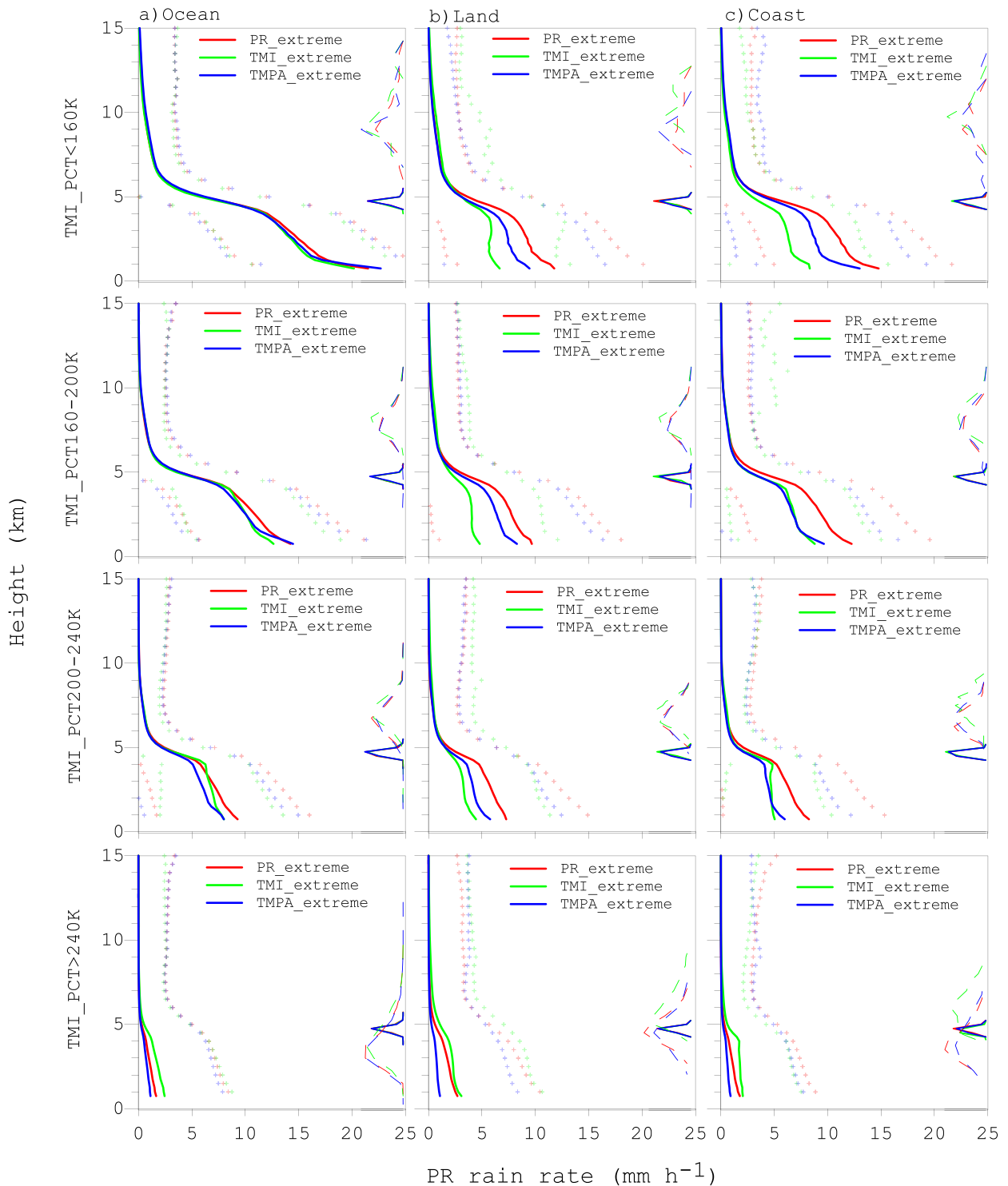
FIG. 8. Collocated PR 2A25 vertical rain-rate mean for PR uppermost 1% extremes (red), TMI uppermost 1% extremes (green), and TMPA uppermost 1% extremes (blue), as classified by four TMI minimum 85-GHz PCT ranges [(top) <160, (top middle) 160–200, (bottom middle) 200–240, and (bottom) >240 K] and (a) ocean, (b) land, and (c) coast. The uppermost 1% are obtained using TRMM observations from 1998 to 2014. Plus signs indicate 95% confidence interval. Solid color lines on the right represent the corresponding freezing heights, while dashed ones represent the corresponding PR 2A23 storm-top heights.
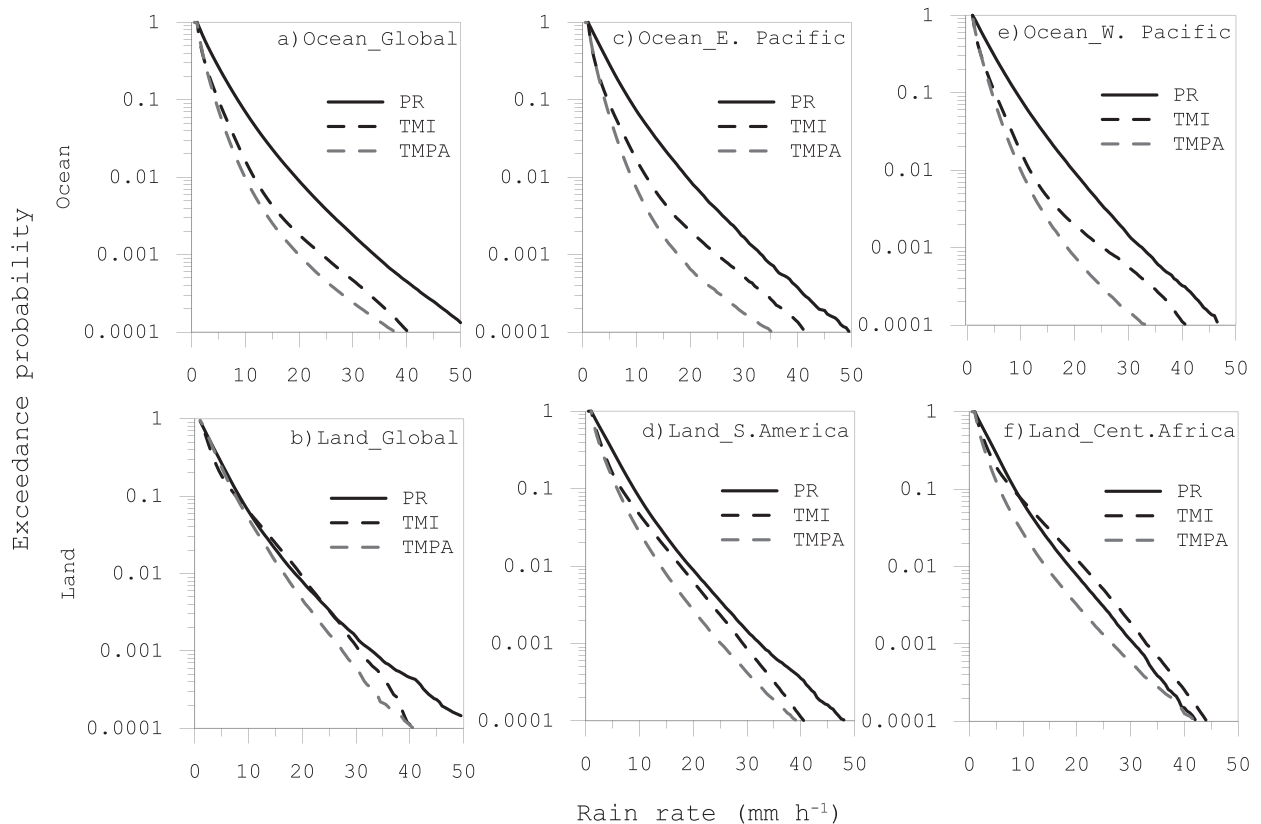
FIG. 9. Comparison of PR (black solid), TMI (black dashed), and TMPA (gray dashed) exceedance probabilities calculated using long-term data from 1998 to 2014 for (a) global ocean, (b) global land, (c) east Pacific (ocean) 90°–130°W, 15°S–15°N, (d) South America (land) 45°–80°W, 35°S–10°N, (e) west Pacific (ocean) 130°–165°E, 5°–20°N, and (f) central Africa (land) 15°–45°E, 15°S–15°N.

using long-term data records from 1998 to 2014. The results revealed that the rain rate in general and in the extreme cases has its own characteristics attributed to the differences: 1) For the nonextreme rain events (below $10 \, \mathrm{mm \, h^{-1}}$), TMI and TMPA have a higher probability of detection than PR over the three surfaces. 2) For moderately heavy rain events (between 10 and $25 \, \mathrm{mm \, h^{-1}}$), the TMI algorithm over land detects more frequent rain events than PR and TMPA. 3) However, the detected extreme events from TMI land algorithm decreased at above $30 \, \mathrm{mm \, h^{-1}}$. Further analysis shows that the TMI extreme events are heavily accompanied with the strongest ice-scattering signals and highest storm-top heights, while the PR extremes show a weaker relationship between the three variables.

The PR–TMI differences in representing the uppermost 1% extremes highlight the known weakness in the TMI land algorithm. The TMI land estimates depend on the existence of ice particles aloft in precipitating clouds since they assume a tight relationship between ice-scattering signals and surface rain rates. Heavy rain events are generally associated with stronger convection, which contains ice particles aloft. However, it has

been shown that the rain-rate–ice-scattering relationship is not always robust. Very intense rain events identified by PR are not associated with the highest storm-top height and are thus unlikely with the most abundant ice particles aloft. The comparison with the global exceedance probability provided in the previous section indicates that higher extreme events are not necessarily accompanied by extreme ice-scattering signals, similar to Hamada et al. (2015), while the TMI land algorithm by design always predicts the heaviest rains from the lowest PCT. The factors contributing to the higher PR extremes are now under investigation.

There are several remarks related to this study. First, despite the PR–TMI extreme contrast over land, it appears that both estimates are statistically consistent over ocean, which is possibly due to the use of both emission and ice-scattering channels for TMI. Second, although TMI often provides similar results as TMPA for light rain rates, there are large estimation differences for medium to heavy rain events, particularly over ocean and coast. Comparison of the uppermost 1% yields higher conformity between PR and TMPA in terms of ice-scattering signals, storm-top heights, and vertical rain profiles.

However, the results also suggest that extreme events from both of the sources are not quite similar, although TMPA tends to provide rain estimates between PR and TMI. The main reason between this difference is still unclear. It is possible that the temporal mismatch between instantaneous PR rainfall and 3-hourly snapshot rain data from TMPA may have a significant contribution to this condition (Prakash et al. 2012). Further, since the extreme cases are selected from 1% of the upper distribution, the large number of very light rain events from TMPA could also introduce a bias to the 1% threshold, which determines the extremes. Changing the 1% extreme threshold into a higher specific value does increase the TMPA extreme means. However, a similar comparison using two specific thresholds (10 and 15 $mm\,h^{-1}$) shows no significant differences in the extreme properties, particularly the vertical rain-rate profiles.

REFERENCES

Adhikari, P., Y. Hong, K. R. Douglas, D. B. Kirschbaum, J. Gourley, R. Adler, and G. R. Brakenridge, 2010: A digitized global flood inventory (1998–2008): Compilation and preliminary results. *Nat. Hazards*, **55**, 405–422, doi:10.1007/ s11069-010-9537-2.

Aldrian, E., and R. Dwi Susanto, 2003: Identification of three dominant rainfall regions within Indonesia and their relationship to sea surface temperature. *Int. J. Climatol.*, **23**, 1435–1452, doi:10.1002/joc.950.

As-Syakur, A. R., T. Tanaka, T. Osawa, and M. S. Mahendra, 2013: Indonesian rainfall variability observation using TRMM multi-satellite data. *Int. J. Remote Sens.*, **34**, 7723–7738, doi:10.1080/01431161.2013.826837.

Berg, W., T. L'Ecuyer, and C. Kummerow, 2006: Rainfall climate regimes: The relationship of regional TRMM rainfall biases to the environment. *J. Appl. Meteor. Climatol.*, **45**, 434–454, doi:10.1175/JAM2331.1.

Chang, C.-P., Z. Wang, J. McBride, and C.-H. Liu, 2005: Annual cycle of Southeast Asia–Maritime Continent rainfall and the asymmetric monsoon transition. *J. Climate*, **18**, 287–301, doi:10.1175/JCLI-3257.1.

Fu, Y., and G. Liu, 2003: Precipitation characteristics in midlatitude East Asia as observed by TRMM PR and TMI. *J. Meteor. Soc. Japan*, **81**, 1353–1369, doi:10.2151/jmsj.81.1353.

Furuzawa, F. A., and K. Nakamura, 2005: Differences of rainfall estimates over land by Tropical Rainfall Measuring Mission (TRMM) Precipitation Radar (PR) and TRMM Microwave Imager (TMI)—Dependence on storm height. *J. Appl. Meteor.*, **44**, 367–383, doi:10.1175/JAM-2200.1.

Gopalan, K., N.-Y. Wang, R. Ferraro, and C. Liu, 2010: Status of the TRMM 2A12 land precipitation algorithm. *J. Atmos. Oceanic Technol.*, **27**, 1343–1354, doi:10.1175/ 2010JTECHA1454.1.

Habib, E., A. Henschke, and R. F. Adler, 2009: Evaluation of TMPA satellite-based research and real-time rainfall estimates during six tropical-related heavy rainfall events over Louisiana, USA. *Atmos. Res.*, **94**, 373–388, doi:10.1016/ j.atmosres.2009.06.015.

Hamada, A., Y. N. Takayabu, C. Liu, and E. J. Zipser, 2015: Weak linkage between the heaviest rainfall and tallest storms. *Nat. Commun.*, **6**, 6213, doi:10.1038/ncomms7213.

Huffman, G. J., and D. T. Bolvin, 2013: TRMM and other data precipitation data set documentation. NASA TRMM Doc., 40 pp.

——, and Coauthors, 2007: The TRMM Multisatellite Precipitation Analysis (TMPA): Quasi-global, multiyear, combined-sensor precipitation estimates at fine scales. *J. Hydrometeor.*, **8**, 38–55, doi:10.1175/JHM560.1.

Ichikawa, H., and T. Yasunari, 2006: Time–space characteristics of diurnal rainfall over Borneo and surrounding oceans as observed by TRMM-PR. *J. Climate*, **19**, 1238–1260, doi:10.1175/ JCLI3714.1.

Iguchi, T., and R. Meneghini, 1994: Intercomparison of single-frequency methods for retrieving a vertical rain profile from airborne or spaceborne radar data. *J. Atmos. Oceanic Technol.*, **11**, 1507–1516, doi:10.1175/1520-0426(1994)011<1507: IOSFMF>2.0.CO;2.

——, T. Kozu, R. Meneghini, J. Awaka, and K. Okamoto, 2000: Rain-profiling algorithm for the TRMM Precipitation Radar. *J. Appl. Meteor.*, **39**, 2038–2052, doi:10.1175/ 1520-0450(2001)040<2038:RPAFTT>2.0.CO;2.

Kiktev, D., D. M. Sexton, L. Alexander, and C. K. Folland, 2003: Comparison of modeled and observed trends in indices of daily climate extremes. *J. Climate*, **16**, 3560–3571, doi:10.1175/ 1520-0442(2003)016<3560:COMAOT>2.0.CO;2.

Kripalani, R. H., and A. Kulkarni, 1997: Rainfall variability over South-east Asia—Connections with Indian monsoon and ENSO extremes: New perspectives. *Int. J. Climatol.*, **17**, 1155–1168, doi:10.1002/(SICI)1097-0088(199709)17:11<1155:: AID-JOC188>3.0.CO;2-B.

Kumar, R., A. Varma, A. Mishra, R. Gairola, I. Das, A. Sarkar, and V. Agarwal, 2009: Comparison of TRMM TMI and PR version 5 and 6 precipitation data products under cyclonic weather conditions. *IEEE Trans. Geosci. Remote Sens. Lett.*, **6**, 378–382, doi:10.1109/LGRS.2009.2014257.

Kummerow, C., and L. Giglio, 1994: A passive microwave technique for estimating rainfall and vertical structure information from space. Part I: Algorithm description. *J. Appl. Meteor.*, **33**, 3–18, doi:10.1175/1520-0450(1994)033<0003:APMTFE>2.0.CO;2.

——, W. S. Olson, and L. Giglio, 1996: A simplified scheme for obtaining precipitation and vertical hydrometeor profiles from passive microwave sensors. *IEEE Trans. Geosci. Remote Sens.*, **34**, 1213–1232, doi:10.1109/36.536538.

——, W. Barnes, T. Kozu, J. Shiue, and J. Simpson, 1998: The Tropical Rainfall Measuring Mission (TRMM) sensor package. *J. Atmos. Oceanic Technol.*, **15**, 809–817, doi:10.1175/ 1520-0426(1998)015<0809:TTRMMT>2.0.CO;2.

——, and Coauthors, 2001: The evolution of the Goddard profiling algorithm (GPROF) for rainfall estimation from passive microwave sensors. *J. Appl. Meteor.*, **40**, 1801–1820, doi:10.1175/1520-0450(2001)040<1801:TEOTGP>2.0.CO;2.

Liu, J., C. D. Doan, S.-Y. Liong, R. Sanders, A. T. Dao, and T. Fewtrell, 2015: Regional frequency analysis of extreme rainfall events in Jakarta. *Nat. Hazards*, **75**, 1075–1104, doi:10.1007/s11069-014-1363-5.

Masunaga, H., T. Iguchi, R. Oki, and M. Kachi, 2002: Comparison of rainfall products derived from TRMM microwave imager and precipitation radar. *J. Appl. Meteor.*, **41**, 849–862, doi:10.1175/1520-0450(2002)041<0849:CORPDF>2.0.CO;2.

——, T. S. L'Ecuyer, and C. D. Kummerow, 2005: Variability in the characteristics of precipitation systems in the tropical Pacific. Part I: Spatial structure. *J. Climate*, **18**, 823–840, doi:10.1175/JCLI-3304.1.

Mori, S., and Coauthors, 2004: Diurnal land–sea rainfall peak migration over Sumatera Island, Indonesian Maritime Continent, observed by TRMM satellite and intensive rawinsonde soundings. *Mon. Wea. Rev.*, **132**, 2021–2039, doi:10.1175/1520-0493(2004)132<2021:DLRPMO>2.0.CO;2.

NASA, 2011a: TRMM product level 2A Precipitation Radar (PR) rainfall rate and profile, version 7.00. GES DISC, accessed 22 March 2015. [Available online at https://disc.sci.gsfc.nasa.gov/precipitation/documentation/TRMM_README/TRMM_2A25_readme.shtml.]

——, 2011b: TRMM Microwave Imager (TMI) level 2A hydrometeor profile product, version 7.00. GES DISC, accessed 22 March 2015. [Available online at https://disc.gsfc.nasa.gov/precipitation/documentation/TRMM_README/TRMM_2A12_readme.shtml.]

——, 2011c: TRMM product 3B42, version 7.00. GES DISC, accessed 22 March 2015. [Available online at https://disc.gsfc.nasa.gov/precipitation/documentation/TRMM_README/TRMM_3B42_readme.shtml.]

——, 2011d: TRMM Microwave Imager (TMI) level 1B calibrated brightness temperature (TB) product, version 7.00. GES DISC, accessed 22 March 2015. [Available online at https://disc.gsfc.nasa.gov/precipitation/documentation/TRMM_README/TRMM_1B11_readme.shtml.]

——, 2011e: TRMM product level 2A Precipitation Radar (PR) rain characteristics (2A23), version 7.00. GES DISC, accessed 22 March 2015. [Available online at https://disc.gsfc.nasa.gov/precipitation/documentation/TRMM_README/TRMM_2A23_readme.shtml.]

Nesbitt, S. W., E. J. Zipser, and D. J. Cecil, 2000: A census of precipitation features in the tropics using TRMM: Radar, ice scattering, and lightning observations. *J. Climate*, **13**, 4087–4106, doi:10.1175/1520-0442(2000)013<4087:ACOPFI>2.0.CO;2.

Prakash, S., C. Mahesh, R. M. Gairola, and P. K. Pal, 2012: Comparison of high-resolution TRMM-based precipitation products during tropical cyclones in the north Indian Ocean. *Nat. Hazards*, **61**, 689–701, doi:10.1007/s11069-011-0055-7.

Qian, J.-H., 2008: Why precipitation is mostly concentrated over islands in the Maritime Continent. *J. Atmos. Sci.*, **65**, 1428–1441, doi:10.1175/2007JAS2422.1.

Rajendran, K., and T. Nakazawa, 2005: Systematic differences between TRMM 3G68 PR and TMI rainfall estimates and the possible association with life cycle of convection. *SOLA*, **1**, 165–168, doi:10.2151/sola.2005-043.

Ramage, C. S., 1968: Role of a tropical ''Maritime Continent'' in the atmospheric circulation. *Mon. Wea. Rev.*, **96**, 365–370, doi:10.1175/1520-0493(1968)096<0365:ROATMC>2.0.CO;2.

Rosenfeld, D., 2007: Cloud top microphysics as a tool for precipitation measurements. *Measuring Precipitation from Space*, Springer, 61–77.

Salahuddin, A., and S. Curtis, 2011: Climate extremes in Malaysia and the equatorial South China Sea. *Global Planet. Change*, **78**, 83–91, doi:10.1016/j.gloplacha.2011.05.001.

Seto, S., and T. Iguchi, 2007: Rainfall-induced changes in actual surface backscattering cross sections and effects on rain-rate estimates by spaceborne precipitation radar. *J. Atmos. Oceanic Technol.*, **24**, 1693–1709, doi:10.1175/JTECH2088.1.

Spencer, R. W., H. M. Goodman, and R. E. Hood, 1989: Precipitation retrieval over land and ocean with the SSM/I: Identification and characteristics of the scattering signal. *J. Atmos. Oceanic Technol.*, **6**, 254–273, doi:10.1175/1520-0426(1989)006<0254:PROLAO>2.0.CO;2.

Tangang, F. T., L. Juneng, E. Salimun, P. N. Vinayachandran, Y. K. Seng, C. J. C. Reason, S. K. Behera, and T. Yasunari, 2008: On the roles of the northeast cold surge, the Borneo vortex, the Madden-Julian oscillation, and the Indian Ocean dipole during the extreme 2006/2007 flood in southern peninsular Malaysia. *Geophys. Res. Lett.*, **35**, L14S07, doi:10.1029/2008GL033429.

TRMM PR Team, 2011: Tropical Rainfall Measuring Mission (TRMM) Precipitation Radar algorithm: Instruction manual for version 7. JAXA/NASA Tech. Rep., 170 pp. [Available online at http://www.eorc.jaxa.jp/TRMM/documents/PR_algorithm_product_information/pr_manual/PR_Instruction_Manual_V7_L1.pdf.]

Zagrodnik, J. P., and H. Jiang, 2013: Investigation of PR and TMI version 6 and version 7 rainfall algorithms in landfalling tropical cyclones relative to the NEXRAD stage-IV multi-sensor precipitation estimate dataset. *J. Appl. Meteor. Climatol.*, **52**, 2809–2827, doi:10.1175/JAMC-D-12-0274.1.